ADVANCED ELECTRONIC MATERIALS Open Access
www.advelectronicmat.de

Local Fermi Level Engineering in 2D-MoS_2 Realized via Microcontact Printing of Self-Assembled Monolayers for Next-Generation Electronics

Sarah Grützmacher, Max Heyl, Norbert Koch, Emil J. W. List-Kratochvil, and Giovanni Ligorio**

Silicon-based technology is approaching scalability limits due to severe short-channel effects arising from its intrinsic bulk properties. In contrast, two-dimensional (2D) transition metal dichalcogenides (TMDCs) exhibit remarkable resilience to these effects because of their atomic-scale thickness, positioning them as promising candidates for next-generation optical and electronic devices. However, realizing 2D material-based technology still requires the development of local p- and n-type doping methods essential for complementary circuits. Self-assembled monolayers (SAMs) have shown the ability to locally engineer electronic energy levels in 2D TMDCs to address this challenge. In this study, we demonstrate local engineering of electronic energy levels on micrometer scale in semiconducting single-layer (1L) MoS_2 by patterning the supporting substrate with functional SAMs via microcontact printing (μCP). Three SAMs were selected: two with large opposing dipole moments and one non-dipolar reference. Their impact on surface properties particularly the work function and on optoelectronic properties of 1L-MoS_2 was investigated via Kelvin probe microscopy and photoluminescence (PL) mapping. Significant shifts in work function and PL were observed. FETs fabricated on locally patterned substrates enabled direct comparison, confirming that threshold voltage shifts up to 80 V and ON-current increases by two orders of magnitude arise solely from SAM polarity. This work demonstrates that μCP and the electrostatic doping capabilities of dipolar SAMs offer a straight forward and scalable approach to locally engineering 1L-MoS_2 energy levels.

1. Introduction

For the ever-growing demand for smaller, faster, and more energy-efficient electronics, conventional silicon-based complementary metal-oxide-semiconductor (CMOS) technology is reaching its performance limits.[1,2] At nanometer scale, the 3D bulk semiconductor silicon suffers from short-channel effects, resulting in heat dissipation and elevated energy consumption in the OFF-state of field-effect transistors (FETs). Furthermore, substitutional doping, employed to obtain p- or n-type FETs for CMOS (complementary metal oxide semiconductor) applications, is plagued by fluctuations in the doping concentration at this small scale, unwantedly shifting the threshold voltage.[1–7] 2D transition metal dichalcogenides (TMDCs) have emerged as an outstanding candidate to substitute silicon due to their layered nature, allowing down-scaling to three-atom thick single layers (1Ls) without significant loss in electric performance.[2,4,8–11] However, the material's 2D nature prevents traditional techniques of semiconductor

S. Grützmacher, M. Heyl, N. Koch, E. J. W. List-Kratochvil, G. Ligorio
Humboldt-Universität zu Berlin
Institut für Physik
Institut für Chemie
Zum Großen Windkanal 2, 12489 Berlin, Germany
E-mail: emil.list-kratochvil@hu-berlin.de; giovanni.ligorio@hu-berlin.de

N. Koch, E. J. W. List-Kratochvil
Helmholtz-Zentrum Berlin für Materialien und Energie GmbH
Hahn-Meitner-Platz 1, 14109 Berlin, Germany

E. J. W. List-Kratochvil, G. Ligorio
Center for the Science of Materials Berlin
Zum Großen Windkanal 2, 12489 Berlin, Germany

The ORCID identification number(s) for the author(s) of this article can be found under https://doi.org/10.1002/aelm.202500081

DOI: 10.1002/aelm.202500081

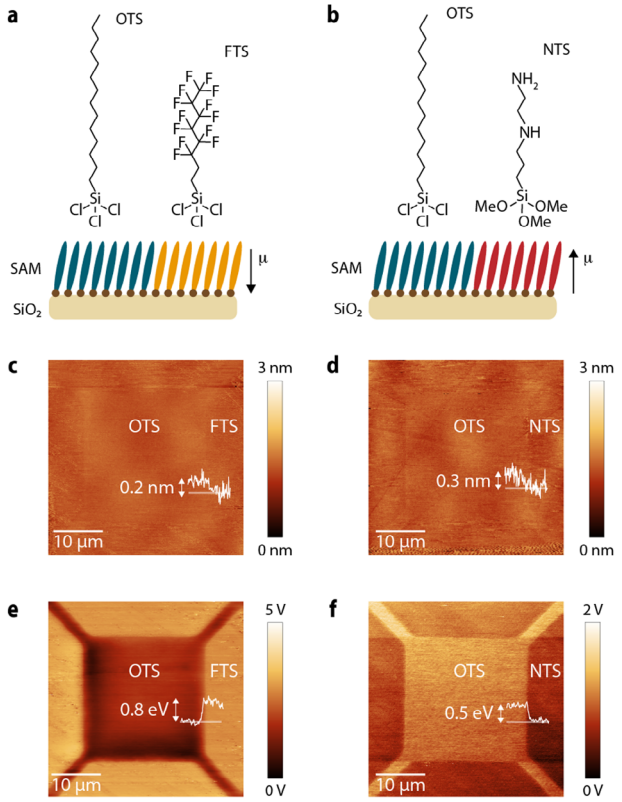

Figure 1. a,b) Schematic and chemical structure of FTS/OTS- and NTS/OTS-SAM treated substrates, respectively. c,d) SFM image FTS/OTS and NTS/OTS SAM pattern. The inset lines represent the height measured locally. e,f) Respective KPFM images of FTS/OTS- and NTS/OTS-SAM pattern, displaying a difference in V_{CPD} of $\Delta^{KPFM}_{OTS-FTS} = 0.8$ V and $\Delta^{KPFM}_{OTS-NTS} = 0.5$ V respectively.

doping, necessitating the exploration of novel methods. For CMOS technology, both p- and n-type doping must be achieved in close proximity on a sub-micrometer scale. The sensitivity of 1L-TMDCs to their environment, particularly to modifications in the substrate's dielectric properties, offers a promising approach to engineering electronic energy levels. By altering the surroundings – such as chemically modifying the substrate, rather than the material itself, as in silicon technology – the optical and electrical behavior of 1L-TMDCs can be finely tuned. Studies have shown that chemical modifications of the substrate can yield drastic effects on TMDCs, impacting parameters such as their work function (Φ),[12–20] the optical and electronic bandgap (E_g),[21–26] and, as a result, the photoluminescence (PL).[27–31]

In this work, we employ microcontact printing (μCP), a simple and scalable process, to locally modify the TMDC-supporting substrates with self-assembled monolayers (SAMs). SAMs feature densely packed molecules with uniform orientation. They consist of an anchoring group, which selectively binds to the substrate, and a mostly hydrocarbon-based functional group. The latter can be designed to specifically modify the surface properties, for instance, by introducing permanent molecular dipoles. Due to the nearly-parallel alignment of the molecules forming the SAM and the perpendicular orientation to the substrate, the collectively aligned individual molecular dipoles result in a macroscopic surface dipole, thus changing the substrate's work function (Φ_{sub}).[32–34] By patterning two distinct SAMs with opposing dipole moment directions, we establish a pattern of locally varying work functions on the substrate surface. When a 1L-TMDC is placed on the SAM-patterned substrate, its optical and electronic properties undergo local changes based on the SAM it is in contact with. In previous work, we demonstrated that the SAMs not only induce a shift in the TMDC's Fermi Level(E_F) within the E_g but that the E_g itself is renormalized.[21–26,35,36] The shift of E_F itself was found to be dependent on the SAM's dipole orientation. A SAM with a downward-oriented dipole(with respect to the substrate surface) shifts the E_F toward the valence band(VB), while a SAM with an upward-oriented dipole shifts it toward the conduction band(CB). The renormalization of E_g is due to the dielectric contrast between the 2D semiconductor in its environment, i.e., the SAM, and is thus dependent on the dielectric constant of the SAMs.[32,37]

In this study, we extend our previous investigation by comparing SAMs with opposing dipole moments and implementing local control of the semiconductor's electronic properties in devices. We apply μCP to pattern our substrates with two SAMs and transfer large flakes MoS_2 on top. This enables us to build devices on a single-flake MoS_2 on two different SAMs. Compared to our previous work, here we also investigate the impact of the SAMs on FET characteristics such as threshold voltage (V_{th}), mobility (μ), and charge carrier density (n), thereby avoiding possible flake-to-flake variations in MoS_2 native quality. The FET characteristics confirm the reliable engineering of the 1L-MoS_2 energy levels on the micrometer scale within one flake. The approach presented here could pave the way to integrate 2D TMDCs into alternative CMOS technology.

2. Results and Discussion

2.1. Modification of Substrates via Microcontact Printing of SAMs

Three SAMs were selected based on their intrinsic molecular dipoles: one with downward-oriented dipole moment, one with a negligible dipole moment ("non-dipolar") and one with an upward-oriented dipole moment – all with respect to the substrate surface. The SAMs with the downward- and upward-oriented dipoles were selected to modify the electrostatic potential of the substrate (and later the energy levels of MoS_2), while the non-dipolar SAM served as internal standard. The three SAMs were paired to achieve two combinations: one paired the SAM with downward-oriented dipole with the non-dipolar SAM, the other paired the SAM with the upward-oriented dipole with the non-dipolar SAM. This way, the SAMs with the downward- and upward-oriented dipoles are referenced to the internal standard. The molecules selected for SAM formation based on their molecular dipoles were trichloro(1,1,2,2-perfluorooctyl)silane (FTS) with a downward-oriented dipole moment, non-dipolar octadecyltrichlorosilane (OTS), and [3-(2-aminoethylamino)-propyl]trimethoxysilane (NTS) with upward-oriented dipole moment. The molecules were paired in patterns to achieve the two combinations: FTS/OTS and NTS/OTS.

The substrates (Si/SiO_2 wafers, 300 nm oxide layer) were modified by attaching these two SAM combinations sequentially:

The first SAM was deposited by employing microcontact printing (μCP) to selectively pattern the surface of the substrate, the second SAM via chemical bath deposition to fill the gaps left uncovered by the first SAM.

Figure 1a,b show the chemical structures of the three molecules, alongside a schematic representation of the cross section of the SAM-functionalized SiO_2 substrates. The sketch displays an idealized model of the SAMs on the SiO_2 substrate, indicating the different orientations and magnitude of the respective molecular dipole moments.

The modification of the substrates started by employing OTS, following the procedure previously reported.[38] The SAM molecules consist of a C_{18} carbohydrate chain with an anchoring silane group which binds to the SiO_2 substrate. A theoretical length for the molecule of 2.3 nm was derived via density functional theory (DFT, B3LYP/6-311G(d,p) level of theory). This is well aligned with both theoretical and experimental literature values (2.1–2.6 nm).[39–42] OTS was patterned on the substrates using μCP. For this, we used a PDMS stamp with a pattern of squares (20 μm × 20 μm) connected by diagonal lines (2 μm). The pattern leaves uncovered octagonal gaps on the surface (see experimental details). The gaps were filled with either FTS or NTS by chemical bath deposition (CBD). FTS ($CF_3(CF_2)_5(CH_2)_2SiCl_3$) consists of a perfluorinated C_6 carbon chain, a $(—CH_2)_2$ spacer group and an anchoring silane group. The molecular length calculated via DFT is 1.3 nm (literature reports values between 0.9 nm and 1.4 nm).[17,40,43–46] NTS ($C_8H_{22}N_2O_2Si$) consists of an aminoethyl group bound to an aminopropyl group and an anchoring trimethoxy silane group. The calculated molecular length is 0.8 nm (literature reports values between 0.8 and 1.2 nm).[47,48]

The modification of the substrates with FTS/OTS and NTS/OTS SAMs was investigated via scanning force microscopy (SFM). Figure 1c,d display the SFM images of the FTS/OTS and NTS/OTS patterned substrates, respectively. The inset line in the image reports the height that was measured locally. While the nominal difference in molecular length between FTS and OTS is 1.0 nm, and between NTS and OTS is 1.5 nm, the SFM image only shows a difference of 0.2 and 0.3 nm for FTS/OTS and NTS/OTS, respectively. This discrepancy can be attributed to either a lower packing density of OTS compared to FTS and NTS due to the μCP, or to the larger tilt angle of OTS. In our previous work, we compared the surface free energy modification via contact angle measurements of OTS deposited via μCP and via CBD.[38] We demonstrated that the contact angle measurements for both methods closely aligned with literature values for OTS deposited via CBD, indicating a high degree of similarity.[49–52] The discrepancy in the height between the molecular lengths and SAM films is therefore not attributed to a lack of packing density, but to the larger tilt angle of OTS compared to FTS and NTS. Due to steric and geometric constraints imposed by the fluorine van der Waals radii, perfluoroalkyls have a helical rather than alkyl zigzag structure.[53] This results in more rigid molecules which stand almost perpendicular to the surface. OTS, on the other hand, has been reported to have a tilt angle of up to 50°.[53,54] Contact angle measurements were performed for all three SAMs and can be found in the (see Figure S1, Supporting Information). The values for FTS (113.7° ± 0.2°) and OTS (109.6° ± 0.4°) are in good agreement with literature values for monolayers. Values for NTS (61.2° ± 6.5°) lie between literature values for monolayers (36°) and multilayers (83°).[47,48,55] NTS and similar amine-SAMs are reported to form islands of multilayers due to polymerization.[48,55] We therefore assume partial multilayer formation on our samples.

To assess the homogeneity of the SAMs, scanning electron microscopy (SEM) images were captured at larger scales and random positions on the substrate. Typical images can be found in Figure S2 (Supporting Information). The images show a homogeneous coverage of the SAM over large areas.

The successful deposition of the SAMs was additionally confirmed via X-ray photoelectron spectroscopy (XPS). For this, highly doped p++ type Si substrates with a native oxide layer (≈3 nm) were chosen as substrates to avoid charging during the measurement. Their surfaces were chemically modified with either OTS, FTS or NTS. To meet the lateral detection limitation of XPS, stamps with no features were employed for OTS for full coverage of the sample. FTS and NTS were deposited via CBD analogous to the patterned samples. The results can be found in the supplementary information (see Figure S3, Supporting Information) and report the spectra for carbon [C(1s)], fluorine [F(1s)] and nitrogen [N(1s)]. For OTS, the C(1s) core level consists of one peak centered at 285 eV, attributed to the $–CH_2$ and $–CH_3$ carbons. For FTS, the C(1s) core level consists of two main components with binding energies at 285 eV and 291 eV, which are assigned to the $–CH_2$ and $–CF_2/—CF_3$ groups, respectively. The F(1s) core level is centered at 689 eV. For NTS, the C(1s) and N(1s) core level is centered at 285 and 399 eV, respectively. The broadening of the N(1s) core level is attributed to NH_2 and NH_3^+ species.

The electrical modification of the substrates by the SAMs was investigated by means of Kelvin probe force microscopy (KPFM). Figure 1e,f show the KPFM images obtained simultaneously during the SFM measurement (see Figure 1c,d). The SAM pattern is clearly visible in color contrast, representing the difference in contact potential difference (V_{CPD}). OTS exhibits a reduced V_{CPD} compared to FTS by $\Delta^{KPFM}_{OTS-FTS} = 0.8$ V and an increased V_{CPD} compared to NTS by $\Delta^{KPFM}_{OTS-NTS} = -0.5$ V. The inset line in the images displays the V_{CPD} measured locally. This change in potential of the substrate is caused by the electrostatic potential of the SAMs due to their aligned permanent dipole moments, resulting in a macroscopic change of the surface dipole, and thereby a shift in the electrostatic potential of the substrate.[54,56] This relationship is expressed by the Helmholtz equation as:[54] $\Delta V_{SAM} = \mu_z/A\varepsilon_0\varepsilon_{SAM}$, where ΔV_{SAM} is the SAM-induced shift in potential of the substrate, μ_z the molecular dipole moment of the SAM molecules perpendicular to the surface, A the lateral area per molecule, ε_0 the permittivity of free space and ε_{SAM} the relative permittivity of the SAM. Thus, the Helmholtz equation can be used to validate the shifts in electric potential measured via KPFM based on the molecular dipole moment of the SAM.[54,56]

In our previous work,[38] we demonstrated that the difference in the shift of V_{SAM} by OTS and FTS is due to the large difference in μ_z of the SAMs, originating from relatively neutral C—H bonds in the OTS SAM and highly polar C—F bonds in the FTS SAM. Similar amine-SAMs to our NTS have been reported to exhibit opposing dipole moments with respect to F-SAMs, as a result of the lone pair electrons of NH_2-SAMs.[18] Due to the lack of literature values for the dipole moment of NTS, we calculated

Table 1. Summary of the DFT calculations for molecular length, the total dipole moment (μ_{total}) and the dipole moment perpendicular to the surface (μ_z) for FTS, OTS and NTS.

	length [nm]	μ_{total} [D]	μ_z [D]
FTS	1.3	4.02	−3.53
OTS	2.3	1.46	−0.02
NTS	0.8	2.29	0.54

the gas-phase dipole moments of all three SAM molecules via DFT (B3LYP/6-311G(d,p) level of theory). We employed simplified models for the molecules by replacing the Cl/methoxy group with an OH group. The calculated molecular length, μ_{total} (total dipole moment) and μ_z (dipole moment perpendicular to the surface) are summarized in **Table 1**. The values for μ_{total} and μ_z are in good agreement with literature values for FTS,[54] OTS[40,42] and similar F-,[40,42] alkyl-[34,54] and amine-SAMs.[34,40] It should be noted that literature values vary depending on the models employed for the DFT calculations. Some literature values for OTS, for example, are obtained from more simplified models, where each of the three Cl groups is replaced with hydrogen.[34,54] We find the replacement with an OH group to be more realistic, since the molecules bind to the substrate via Si-O-Si bonds. Nevertheless, we want to emphasize that our calculations primarily indicate trends, which can be used for internal comparison, as they are calculated for the molecules in gaseous-phase in a perfect vacuum.

To quantitatively employ the Helmholtz equation, the lateral area per molecule and dielectric constants of the specific SAM must be known. However, the molecular dipoles can be used for qualitative validation of the KPFM measurements based on the direction and magnitude of the molecular dipoles. The trend of a large negative μ_z for FTS and a positive μ_z for NTS confirms the opposing shifts in Φ_{sub}, observed in our KPFM measurements, where Φ_{sub} is represented by the V_{CPD}. The larger shift of Φ_{sub} by FTS is also relative to its large dipole moment, when compared to the shift of Φ_{sub} by NTS and its smaller dipole moment.

2.2. Local Doping of MoS_2 by SAMs

In our previous work,[38] we investigated local doping effects of FTS and OTS SAM via UPS and PL measurements using two different TMDCs, namely WSe_2 and MoS_2. The FTS SAM exhibited an electron-withdrawing effect, causing a shift of the E_F within the Eg of both TMDCs toward the valence band. In contrast, the OTS SAM had a negligible effect on both TMDCs. We attributed the E_F-shift to the interplay between the dipole change of the underlying substrate and the concurrent modification of the dielectric environment, resulting in a renormalization of the E_g.[26,38] However, what was lacking in our investigation was the exploration of an n-doping SAM, which shifts the E_F toward the conduction band. To address this, we employed the NTS SAM, which is characterized by a dipole moment opposite to that of FTS. To conduct a systematic comparison between FTS and NTS, we utilized the doping-effect-neutral OTS as a reference.

1L-MoS_2 were transferred on FTS/OTS and NTS/OTS modified silicon oxide substrates. The 1Ls were obtained following the previously reported metal-mediated exfoliation process.[38,57,58] This method allows for ultra-large, high-quality single layers. The presence of 1Ls was confirmed via Raman spectroscopy (Figure S4, Supporting Information), where the typical in-plane vibration $E^1{}_{2g}$ and the out-of plane vibration A_{1g} frequency for 1Ls are centered at 390.2 and 408.5 cm^{-1}, respectively.

PL measurements were employed to assess the doping effects that FTS and NTS have on 1L-MoS_2. During PL measurements, excitons are formed in the TMDC. The PL originates from their radiative decay. When the TMDC is n- or p-doped, an additional charge carrier (electron or hole, respectively) can bind to the exciton, generating a trion, which decreases the PL intensity, due to additional non-radiative decay channels.[22,27–31,59,60] Furthermore, trions are characterized by lower emission energies, due to the binding energy of the additional charge carrier. The overlap of exciton and trion emission results in an overall broadened emission band. The doping level of TMDCs, therefore, directly correlates with the PL intensity. An intrinsic TMDC displays maximum PL intensity, while an n- or p-doped TMDC will show decreasing PL with increasing doping levels. Defects such as sulfur vacancies in MoS_2 lead to the natural n-doping nature of this material.

In our previous work,[38] we demonstrated that FTS reduces the n-type character of MoS_2, shifting the E_F away from the conduction band. This also results in a lowering of the trion population. The results are summarized in **Figure 2a**, which schematically displays the PL measurement of 1L-MoS_2 on an FTS/OTS pattern. Due to the reduction in the n-type character, fewer trions are generated in MoS_2 on FTS with respect to OTS, resulting in stronger PL emission. The lower trion population in 1L-MoS_2 on FTS compared to OTS is visible in the color contrast of the PL map displayed in Figure 2b. Each pixel of the map represents the local PL intensity of MoS_2 on the SAM pattern, integrated between 1.6 and 2.1 eV. Figure 2c displays the averaged PL spectra of the map (over a region of 20 × 20 μm^2) for MoS_2 on OTS and FTS. To quantify the trion population, the spectra are deconvoluted into three peaks: the neutral exciton peak X^0 and X^B, which originate from the two spin-split band-edge optical transitions at the K point of the reciprocal lattice, and the negatively charged trion peak X^-.[61,62] Note that the ratio between exciton and trion emission is quantitatively evaluated by comparing the area underneath the X^0 and X^- peaks. Further details on the deconvolution are given in Table S1 (Supporting Information). The impact of the SAMs is evident in the ≈1.5-fold reduction in the intensity of MoS_2 on OTS compared to FTS. Additionally, the PL emission band is broadened on OTS when compared to FTS. Both the reduced PL intensity as well as the broadening of the peak indicate a higher trion-to-exciton ratio on OTS.

Having successfully demonstrated a reduction in the n-type character on FTS compared to OTS, we proceeded to examine whether NTS induces the reverse n-doping effect on 1L-MoS_2. According to our working hypothesis, NTS should lead to a shift of the E_F closer to the conduction band. This should promote the n-type character of the semiconductor and thereby increase the trion population. The results are shown in Figure 2d. The figure again displays the PL measurement of 1L-MoS_2 on NTS/OTS pattern. Due to the n-doping effect of the upward-orientated dipole moment of the NTS-SAM, a weaker PL of MoS_2 on top of NTS is observed with respect to OTS in the PL map. As

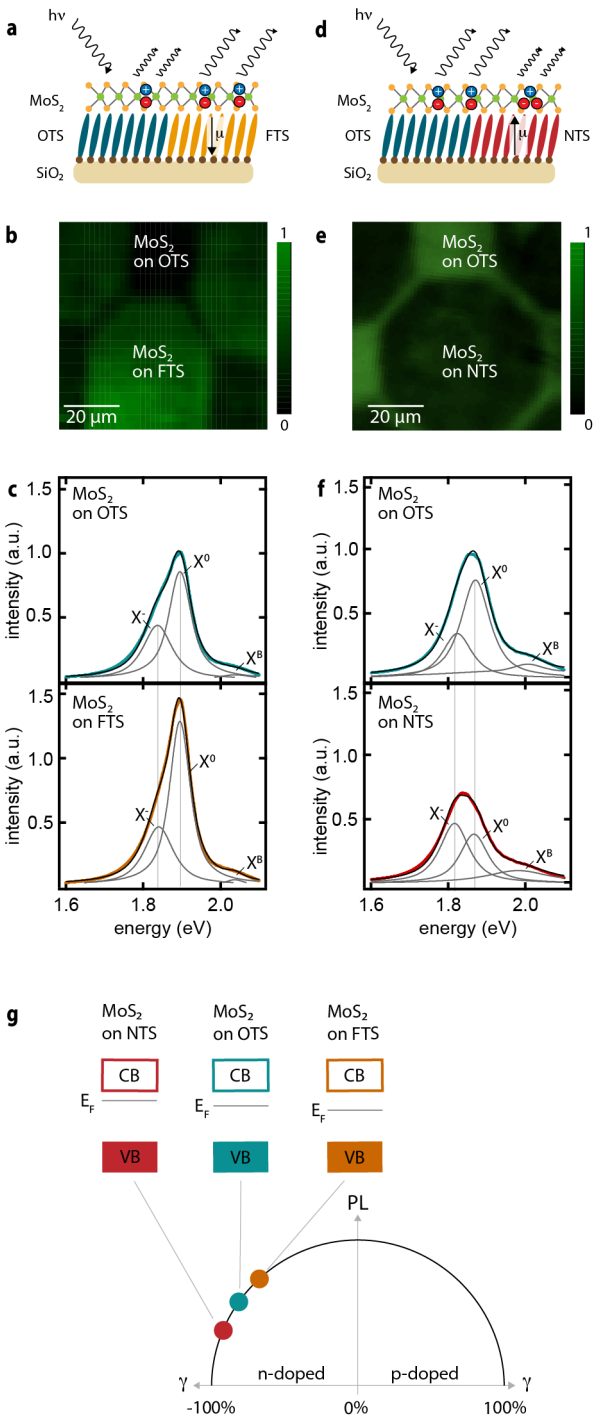

Figure 2. a,d) Schematic of PL measurements of MoS_2 on FTS/OTS- and NTS/OTS-patterned substrates. b,e) PL maps of MoS_2 on FTS/OTS and NTS/OTS pattern, respectively. The brightness of each pixel represents the local PL intensity integrated between 1.6 and 2.1 eV. c,f) Averaged PL spectra of the corresponding PL maps (over a region of 20 × 20 μm^2) of MoS_2 on OTS, FTS, and OTS, NTS. The spectra are deconvolved to demonstrate the distribution of neutral excitons X^0 and negatively charged trions, marked as X^-. The black line corresponds to the cumulative peak fit. g) Schematic of the correlation between the PL intensity and the doping level of MoS_2 on NTS, OTS and FTS. The PL intensity decreases with increased doping level.

expected, the map shows the reverse pattern compared to Figure 2b, displaying brighter PL on OTS relative to NTS. The averaged deconvoluted spectra of MoS_2 on OTS and NTS are displayed in Figure 2f, and further details are given in Table S1 (Supporting Information). MoS_2 shows a ≈1.5-fold enhanced PL on OTS compared to NTS. By deconvoluting the PL spectra, it can be evaluated that the exciton to trion ratio of MoS_2 is increased on OTS with respect to NTS. This clearly demonstrates that the NTS SAM has an n-doping effect on MoS_2 when compared to OTS and FTS. Figure 2g displays a sketch of the correlation between the PL intensity and the doping state of MoS_2. The x-axis represents the doping level of MoS_2. A value of −100% indicates complete n-doping of MoS_2, meaning that the E_F is at the lower edge of the CB. The value of 0% equals intrinsic MoS_2, where the E_F lies in the middle of Eg. The value of 100% indicates complete p-doping of MoS_2, meaning the E_F is at the upper edge of the VB. The y-axis represents the PL-intensity. The dependence of the PL intensity on the doping level is displayed in form of a downward-opened parabola that has its maximum at 0% doping. With increasing doping level, whether n- or p-type, the PL intensity decreases. The lowest PL intensity is observed on NTS, where, due to its n-doping effect, the E_F is closer to the conduction band, relative to OTS and FTS. In contrast, the strongest PL intensity is observed on FTS, where the EF is closer to the VB as a result of the electron-withdrawing nature of the SAM.

2.3. Utilization of FTS, OTS, and NTS in MoS_2 FETs

After characterizing the effects of FTS, OTS, and NTS via PL mapping, we proceeded to showcase the doping effect of the three SAMs in electronic devices by fabricating FETs. Based on PL measurements, the electron withdrawing effect of FTS should reduce the electron concentration in the naturally n-type MoS_2, thereby reducing the conductivity. This should be evident in a shift of the threshold voltage (V_{th}) to higher positive values and lower saturation currents (I_{sat}). Conversely, the n-doping effect of the NTS SAM should increase the electron concentration, increasing the conductivity of MoS_2. This should shift V_{th} to higher negative values and increase I_{sat}.

To compare the different results and quantify the effect of the SAMs, MoS_2 was transferred on FTS/OTS (and NTS/OTS) patterned substrates using results from OTS as a cross reference. This enabled the fabrication of devices on a single flake MoS_2 on both SAMs, eliminating potential influences from differences in MoS_2 quality. Defects, for instance, affect the charge carrier concentration and subsequently influence device characteristics. **Figure 3a** illustrates a schematic of the device cross section of one of the two MoS_2 FETs, namely the one with FTS/OTS pattern. The NTS/OTS device cross section is analogous.

For the fabrication of the devices, highly doped p++ type SiO_2/Si (300 nm) substrates were chemically modified with SAMs following the same procedure discussed above. The substrates served as the bottom gate for the FETs. They were first patterned via μCP (100 × 100 μm squares) with OTS followed by the deposition of FTS (or NTS, see below) via CBD to fill the gaps. 1L-MoS_2 were transferred on to the patterned substrates. Figure 3b shows an optical image of a representative sample. The SAM pattern is visible in the light blue to purple contrast and

ADVANCED ELECTRONIC MATERIALS
Open Access
www.advelectronicmat.de

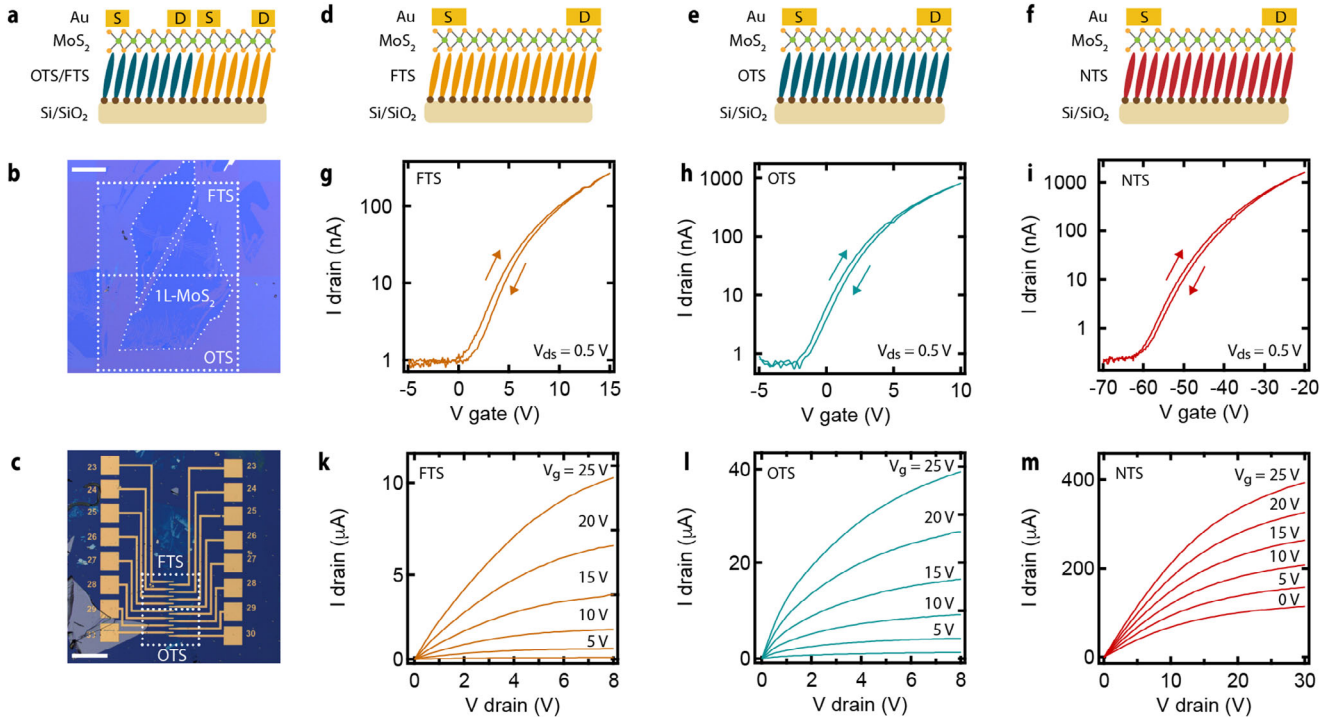

Figure 3. a) Schematic of the cross section of MoS_2 based FETs on FTS/OTS pattern. b) Microscope image of MoS_2 on FTS/OTS square pattern, visible in the blue and purple color contrast and outlined with white dotted squares. 1L-MoS_2 is visible in the darker blue color contrast. c) Optical microscope image of MoS_2 devices on FTS/OTS pattern. The white dotted squares outline the underlying SAM pattern. d–f) Schematic of the cross section of MoS_2 based FETs on FTS, OTS, and NTS, respectively. g–i) Corresponding transfer characteristics of MoS_2 on FTS, OTS, and NTS SAM conducted at V_{ds} = 0.5 V in semi-logarithmic scale. The arrows indicate the sweep direction The V_{th} is shifted to higher negative voltages for increased n-doping by the SAMs from FTS to NTS.(k–m) Output characteristics of MoS_2 FTS, OTS, and NTS, respectively. The output increases with increased n-doping on the NTS SAM. On FTS and OTS the output shape is that of a semiconductor, on NTS that of a resistance due to the high n-doping and resulting high conductivity. The white scale bars in (b,c) correspond to 100 and 300 μm, respectively.

the 1L-MoS_2, covering both SAMs, in the darker blue contrast. Both are outlined with white dotted lines as a visual guide. Source and drain electrodes were fabricated via thermal evaporation of Cr(6 nm)/Au(60 nm) and by using photolithography according to the process described in Figure S5 (Supporting Information), as well as given in the experimental section. For all devices we used channel length L = 50 μm and a channel width W = 30 μm. This procedure enabled us to fabricate multiple devices on a single flake of MoS_2. Annealing at 130 °C for 30 min in a nitrogen atmosphere was conducted to remove water and oxygen and enhance device performance. Figure 3c depicts a sample following the evaporation of source and drain contacts.

Figure 3d–f depicts the schematic representations of the cross-section view of MoS_2 FETs on FTS, OTS, and NTS, respectively. Representative transfer and output characteristics are displayed below each device sketch in Figure 3g–i,k–m, respectively. All measurements were taken in inert nitrogen atmosphere at room temperature. The transfer characteristics display the module of the source-drain current ($|I_{ds}|$) plotted in logarithmic scale against the gate voltage (V_g). The measurement was conducted at a constant source-drain voltage (V_{ds}) of V_{ds} = 0.5 V. The arrows indicate the sweep direction of V_g. The threshold voltage (V_{th}) is extrapolated from the I_{ds}–V_g curves (see Figure S6, Supporting Information). Given the exponential growth of I_{ds}, the curves are plotted both in linear scale and log-log scale. The V_{th} is extrapolated from the intercept between the noise and the current signal in the log-log plot. We observe smaller V_{th} values in the log-log scale compared to the linear plots. Because the noise and the current signal are more clearly visible in the log-log scale, we will only consider and compare the V_{th} values extrapolated from the log-log scale plots. MoS_2 FETs show n-type transconductance on all three SAMs. However, the V_{th} is shifted from 5.2 V on FTS, to −4.4 V on OTS to −52.6 V on NTS. The output characteristics display increasing ON-currents (I_{sat}) from FTS to NTS (FTS<OTS<NTS). The current is increased by up to two orders of magnitude on NTS with respect to FTS (see Figures S8 and S10, Supporting Information). Furthermore, the output characteristics of FTS and OTS FETs have the typical shape observed for most TMDCs, where the I–V curve displays I_{sat} values below 10 nA at a gate voltage of V_g = 0 V. The output curves of NTS, on the other hand, display I_{sat} values ranging from 100 to 500 μA (see Figure S10, Supporting Information) at a gate voltage of V_g = 0 V, clearly demonstrating increased conductance at zero gate voltage. Both the shift in V_{th}, as well as the large increase in I_{sat} on NTS are attributed to enhanced (n-)doping of MoS_2 by the SAMs.

To confirm this assessment, the charge carrier concentration per surface unit (n) was calculated using the parallel-plate capacitor model with $n = C\Delta V_g/e$, where C is the capacitance per surface unit for the silicon oxide substrate given by $C = \varepsilon_0\varepsilon_r/d$,

Table 2. Summary of the carrier mobilities (μ) at the threshold voltage (V_{th}), V_{th} and the charge concentration per surface unit (n) of MoS_2 on FTS, OTS and NTS.

	V_{th} [V]	n [cm^{-2}]	μ [$cm^2\ V^{-1}\ s^{-1}$]
MoS_2 on FTS	8	$2.3 \cdot 10^{12}$	1.4
MoS_2 on OTS	−4	$2.6 \cdot 10^{12}$	2.3
MoS_2 on NTS	−33	$5.2 \cdot 10^{12}$	6.7

$\varepsilon_0 = 8.85 \cdot 10^{-12}$ F m^{-1}, $\varepsilon_r = 3.9$, d = 300 nm, e is the elementary charge and $\Delta V_g = V_g - V_{th}$.[12] As mentioned above, sulfur vacancies in MoS_2 lead to an excess of electrons in the material, giving it a strong n-type character. According to our previous findings discussed above, we expect the FTS SAM to decrease the charge carrier (electron) concentration and the NTS SAM to increase it. Our calculations (summarized in **Table 2**) show that this is the case. MoS_2 on FTS has a 10% reduced carrier concentration compared to the OTS SAM, while MoS_2 on NTS exhibits a ≈2-fold larger charge carrier concentration with respect to MoS_2 on OTS. The results are well aligned with literature values for MoS_2 on similar SAMs.[12,59] The difference in carrier concentration of MoS_2 on the three different SAMs also aligns with the magnitude of the shift in V_{th}, where the largest shift is observed in devices on NTS, and the up to two order of magnitude larger ON-current in the MoS_2-NTS devices.

The carrier mobility (μ) of the FETs was extracted using the equation:

$$\mu = [L/(W(\varepsilon_0\varepsilon_r/d)(\frac{\varepsilon_0\varepsilon_r}{d}V_{ds})] \cdot [dI_{ds}/dV_g] \quad (1)$$

where L, W, and d are the channel length, width, and thickness of SiO_2, and ε_r for SiO_2 corresponds to 3.9. Values for μ at the V_{th} are given in Table 2. Further information on the mobilities plotted over the entire range of V_g can be found in the μ-V_g plot in Figure S7 (Supporting Information). It should be mentioned that the obtained values do not consider the contact resistance at the Au/Cr/MoS_2 interface. Therefore no further quantitative interpretation of the obtained values is provided.

Devices fabricated on MoS_2 on FTS and OTS showed high reproducibility, as can be seen in Figures S8 and S9 (Supporting Information). The Figures display additional output and transfer curves, where characteristics such as V_{th} only showed slight variations from device to device and from flake to flake. For devices fabricated on MoS_2 on NTS, the V_{th} of most devices is between −50 and −60 V. However, devices varied by up to 20 V, the highest being −53 V, the lowest −73 V (see Figure S10, Supporting Information). This variation is attributed to multilayer formation of NTS, indicated by the contact angle measurements (see Figure S1, Supporting Information). Devices with larger $|V_{th}|$ are likely fabricated on MoS_2 on multilayer NTS.

3. Conclusion

We have successfully demonstrated the precise local EF-engineering of 1L-MoS_2 at the lateral microscale. This achievement was enabled by functionalizing SiO_2 substrates using microcontact printing of SAMs with tailored dipole moments. By selecting SAM molecules with opposing dipole orientations relative to the substrate surface, we achieved a macroscopic modulation of the substrate work function. This modulation induced electrostatic doping in 1L-MoS_2, leading to controlled shifts of the EF , either lowering it or raising it toward the conduction band. Our results provide further evidence for the strong correlation between the doping states of TMDCs and their optical properties, such as PL and work function. Specifically, the PL enhancement observed for MoS_2 on the fluorinated SAM substrates is directly linked to a lowered EF, while the PL suppression achieved with the oppositely polarized SAM indicates a shift of the EF closer to the conduction band.

This concept was further validated in FETs based on 1L-MoS_2 on the differently functionalized surfaces. The devices exhibited significant threshold voltage shifts of up to 80 V, a two-fold increase in carrier density, and a 100-fold enhancement in ON-state current. These findings underline the capability to precisely manipulate the EF and enhance the n-type doping character in 1L-MoS_2, thus demonstrating a scalable approach for tailoring the electronic properties of TMDC-based devices. The presented strategy opens a pathway for the development of locally engineered, TMDC-based electronic components as a potential alternative to conventional silicon CMOS technology. While the intrinsic n-type behavior of MoS_2 currently restricts the realization of p-type devices, we anticipate that selecting materials with a more pronounced intrinsic doping character will enable the integration of complementary p- and n-type devices. This technological advancement could facilitate the implementation of TMDCs in next-generation nanoscale electronic and optoelectronic systems.

4. Experimental Section

Sample Cleaning: Highly doped Si wafer (Sigert Wafer, <100>, 525 μm thickness) with a thermally grown oxide layer (300 nm) were cleaned in an ultrasonic bath in deionized water, acetone, and isopropyl alcohol and then dried under nitrogen flow. Afterward the substrates were plasma cleaned (0.35 mbar O_2, 5 min, Diener Plasma cleaner) to remove hydrocarbon contamination and activate the SiO_2 surface for SAM formation.

Microcontact Printing of SAMs: Stamps for the μCP were fabricated by mixing PDMS (Sylgard 184, Dow Corning) and a cross-linker (Sylgard 184, 10 m%). The mixture was stirred for 1 min and evacuated for 5 min at 10^{-2} mbar to remove air bubbles. The mixture was then cast over a stamp master, which is patterned with the features to be replicated on the stamp. The stamp was cured via a baking step (100 °C, 1 hour). For the "SAM-ink", OTS (160 μL) was diluted in hexane (20 mL). The stamp was dipped into the ink (15 s), dried under nitrogen flow (30 s) and pressed on to the freshly plasma-cleaned substrates (10 s). The samples were placed on a hotplate (100 °C, 5 min), cleaned with a Q-tip (dipped in hexene) followed by sonication in toluene and isopropyl alcohol. For the backfilling, the samples were placed in a FTS/NTS solution (60 μg FTS in 20 mL hexene or 80 μL NTS in 20 mL water) overnight, before being placed on the hotplate (100 °C, 10 min).

Metal Exfoliation Substrates: The fabrication of a smooth gold surface needed for metal-assisted exfoliation followed the procedure as previously reported.[57,63] 150 nm Au and 1000 nm Cu was deposited on Silicon wafers (Sigert Wafer, <100>, 525 μm thickness) via physical vapor deposition (≈1.0 Å s^{-1} at 10^{-6} mbar). Glass substrates were fixed onto the metal coated Si wafers with UV-curable epoxy resin (Osilla Encapsulation Epoxy S132).

Metal-Assisted Exfoliation: MoS_2 (2D semiconductors, synthetic crystal) was cleaved with heat resistant Kapton tape and transferred onto the

freshly template-stripped metal substrate. After annealing (200 °C, 120 s) the Kapton tape was removed from the substrate, leaving SL-MoS_2 on the gold substrate.

Polystyrene-Assisted Transfer: MoS_2 on Au was transferred following a reported process.[64] Polystyrene (Sigma–Aldrich, $M_W \approx 280.000$, 90 mg mL^{-1} in toluol) was spin coated (3000 rpm, 60 s) onto the TMDC/Au substrates following a curing step (80 °C, 5 min). The samples were left on a metal etchant (KI_2/I_2 Sigma–Aldrich) until the polystyrene/MoS_2 film floated on top of the solution (≈48 h). To clean off etchtant residue the film was transferred onto deionized water. For the transfer, the film was placed onto isopropyl alcohol and fished out with the target substrate. The samples were dried at room temperature (≈2 h) followed by an annealing step (150 °C, 30 min). The polystyrene was removed with hot toluene (90 °C) followed by rinsing with acetone and isopropyl alcohol.

Contact Angle Measurements: Static contact angle measurements were carried out (DSA100E from Krüss) using the sessile drop method with deionized water.

Scanning Force and Kelvin Probe Force Measurements: SFM/KPFM was performed in air with a Brunker Dimension Icon using PeakForce Tapping with a PFQNE-AL tip (Brunker).

Raman and Photoluminescence Measurements: Raman and PL spectroscopy was performed using a confocal microscope setup (Horiba Ldt.) with a 532 nm Laser excitation source and 20× objective (≈3 µm laser spot size) using an 1800 and 600 L mm^{-1} grating, respectively. The measurements were performed in ambient conditions.

Scanning Electron Microscopy: SEM measurements were performed on a RAITH eLINE Plus microscope operating at 10 kV.

Photolithography: Photolithography was performed employing a maskless aligner (Heidelberg µMLA, 390 nm LED light source). LOR and ECI3007 resists (MicroChemicals) were subsequently spin coated (4000 rpm, 180 s) and heat treated (180 °C and 100 °C, respectively). After the lithography process (115mJ/-9 def), AZ 726 MIF (MicroChemicals) was used as developer (90 s) and deionized water to stop the developing process and rinse the substrate. The remover was rem-700 (MicroChemicals). All lithography steps were performed in a clean room with controlled humidity and temperature.

Devices: MoS_2 based FET devices were fabricated by patterning FTS/OTS or NTS/OTS SAMs via microcontact printing and CBD (as described above) on highly doped p++ type Si/SiO_2 (300 nm oxide) substrates and placing MoS_2 via polystyrene-assisted transfer (see above) on top of the SAM pattern. Source and drain electrodes (Cr(6 nm)/Au(50 nm) were thermally evaporated following photolithography method.

Electronic Transport Measurements: All measurements were performed under inert nitrogen atmosphere. Electrical connections were made using a MPS150 probe station (Cascade) and the device characterization performed using a Keithley 4200A-SCS.

DFT Calculations: Dipole moments normal to the surface (z-axis) for SAM forming molecules were determined using the Gaussian09 software package,[65] applying Density Functional Theory (DFT) with the B3LYP functional and 6–311G(d,p) basis set for calculations. The computational model employed $Si(OH)_3$ to represent silicon anchor groups in a simplified manner.

Statistical Analysis: SFM and KPFM images were processed with the Gwyddion software. For XPS and PL measurements the Igor Pro 9 software from wavemetrics was used and for electrical transport measurements SweepMe! Software was employed.

Supporting Information

Supporting Information is available from the Wiley Online Library or from the author.

Acknowledgements

The authors would like to acknowledge Paul Zybarth and Bodo Kranz for their continuous support in the lab. The authors gratefully acknowledge financial support by the Deutsche Forschungsgemeinschaft through CRC 951 (Project number 182087777). This work was carried out in the framework of the Joint Lab GEN_FAB and was supported by the HySPRINT Innovation Lab at Helmholtz-Zentrum Berlin. The authors would like to thank Prof. Rabe for granting access to laboratory facilities.

Conflict of Interest

The authors declare no conflict of interest.

Data Availability Statement

The data that support the findings of this study are available from the corresponding author upon reasonable request.

Keywords

doping, FET, microcontact printing, MoS_2 , SAM, TMDC

Received: January 27, 2025
Revised: March 14, 2025
Published online: May 23, 2025

[1] D. Akinwande, C. Huyghebaert, C.-H. Wang, M. I. Serna, S. Goossens, L.-J. Li, H.-S. P. Wong, F. H. L. Koppens, *Nature* **2019**, *573*, 507.
[2] Y. Liu, X. Duan, Y. Huang, X. Duan, *Chem. Soc. Rev.* **2018**, *47*, 6388.
[3] K. K. Young, *IEEE Transactions of Electron Dev.* **1998**, *36*, 399.
[4] C. Liu, H. Chen, S. Wang, Q.i Liu, Y.u-G. Jiang, D. W. Zhang, M. Liu, P. Zhou, *Nat. Nanotechnol.* **2020**, *15*, 545.
[5] S. Wang, X. Liu, P. Zhou, *Adv. Mater.* **2022**, *34*, 2106886.
[6] T. Irisawa, O. Numata, T. Tezuka, N. Sugiyama, S.-i. Takagi, *2006 International Electron Devices Meeting*, IEEE, Piscataway, NJ **2006**.
[7] K. Uchida, H. Watanabe, A. Kinoshita, J. Koga, T. Numata, S. Takagi, Digest. International Electron Devices Meeting, IEEE, Piscataway, NJ **2002**.
[8] D. Jariwala, V. K. Sangwan, L. J. Lauhon, T. J. Marks, M. C. Hersam, *ACS Nano* **2014**, *8*, 1102.
[9] G. Fiori, F. Bonaccorso, G. Iannaccone, T. Palacios, D. Neumaier, A. Seabaugh, S. K. Banerjee, L. Colombo, *Nat. Nanotechnol.* **2014**, *9*, 768.
[10] H. Wang, L. Yu, Y.i-H. Lee, Y. Shi, A. Hsu, M. L. Chin, L.-J. Li, M. Dubey, J. Kong, T. Palacios, *Nano Lett.* **2012**, *12*, 4674.
[11] B. Radisavljevic, A. Radenovic, J. Brivio, V. Giacometti, A. Kis, *Nat. Nanotechnol.* **2011**, *6*, 147.
[12] Y. Li, C.-Y. Xu, P. Hu, L. C. Zhen, *ACS Nano* **2013**, *7*, 7795.
[13] H. Sojoudi, J. Baltazar, L. M. Tolbert, C. L. Henderson, S. Graham, *ACS Appl. Mater. Interfaces.* **2012**, *4*, 4781.
[14] X. Sun, X. Wang, P. Wang, B. Sheng, M.o Li, J. Su, J. Zhang, F. Liu, X. Rong, F. Xu, X. Yang, Z. Qin, W. Ge, B. o. Shen, *Opt. Mater. Express* **2017**, *7*, 904.
[15] E. Zojer, T. C. Taucher, O. T. Hofmann, *Adv. Mater. Interfaces.* **2019**, *6*, 1900581.
[16] M. Salinas, *Interface Engineering with Self-Assembled Monolayers for Organic Electronics*, Vol. *4*, FAU University Press, Germany **2014**.
[17] B. Lee, Y. Chen, F. Duerr, D. Mastrogiovanni, E. Garfunkel, E. Y. Andrei, V. Podzorov, *Nano Lett.* **2010**, *10*, 2427.
[18] W. H. Lee, Y. D. Park, *Adv. Mater. Interfaces.* **2017**, *5*, 1700316.
[19] B. de Boer, A. Hadipour, M. M. Mandoc, T. van Woudenbergh, P. W. M. Blom, *Adv. Mater.* **2005**, *17*, 621.

[20] J. Park, W. i. H. Lee, S. Huh, S. H. Sim, S. B. Kim, K. Cho, B. H. Hong, K. S. Kim, *J. Phys. Chem. Lett.* **2011**, *2*, 841.
[21] A. Raja, A. Chaves, J. Yu, G. Arefe, H. M. Hill, A. F. Rigosi, T. C. Berkelbach, P. Nagler, C. Schüller, T. Korn, C. Nuckolls, J. Hone, L. E. Brus, T. F. Heinz, D. R. Reichman, A. Chernikov, *Nat. Commun.* **2017**, *8*, 15251.
[22] B. o. Liu, W. Zhao, Z. Ding, I. Verzhbitskiy, L. Li, J. Lu, J. Chen, G. Eda, K. P. Loh, *Adv. Mater.* **2016**, *28*, 6457.
[23] M. M. Ugeda, A. J. Bradley, S.u-F. Shi, F. H. da Jornada, Y.i Zhang, D. Y. Qiu, W. Ruan, S.-K. Mo, Z. Hussain, Z.-X. Shen, F. Wang, S. G. Louie, M. F. Crommie, *Nat. Mater.* **2014**, *13*, 1091.
[24] Z. Qiu, M. Trushin, H. Fang, I. Verzhbitskiy, S. Gao, E. Laksono, M. Yang, P. Lyu, J. Li, J. Su, M. Telychko, K. Watanabe, T. Taniguchi, J. Wu, A. H. C. Neto, L.i Yang, G. Eda, S. Adam, J. Lu, *Sci. Adv.* **2019**, *5*, https://doi.org/10.1126/sciadv.aaw2347.
[25] J. Ryou, Y. S. Kim, S. Kc, K. Cho, *Sci. Rep.* **2016**, *6*, 29184.
[26] S. Park, T. Schultz, D. Shin, N. Mutz, A. Aljarb, H. S. Kang, C.-H.o Lee, L.-J. Li, X. Xu, V. Tung, E. J. W. List-Kratochvil, S. Blumstengel, P. Amsalem, N. Koch, *ACS Nano* **2021**, *15*, 14794.
[27] M. Buscema, G. A. Steele, H. S. J. van der Zant, A. Castellanos-Gomez, *Nano Res.* **2015**, *7*, 561.
[28] D.-H.o Kang, M.-S. Kim, J. Shim, J. Jeon, H.-Y. Park, W.-S. Jung, H.-Y. Yu, C.-H. Pang, S. Lee, J.-H. Park, *Adv. Funct. Mater.* **2015**, *25*, 4219.
[29] M. Amani, D. H. Lien, D. Kiriya, J. Xiao, A. Azcatl, J. Noh, S. R. Madhvapathy, R. Addou, S. KC, M. Dubey, K. Cho, R. M. Wallace, S. C. Lee, J. H. He, J. Ager, X. Zhang, E. Yablonovitch, A. Javey, *Sci. Nanomater.* **2015**, *350*, 1065.
[30] Y. Li, Z. Qi, M. Liu, Y. Wang, X. Cheng, G. Zhang, L. Sheng, *Nanoscale* **2014**, *6*, 15248.
[31] S. Mouri, Y. Miyauchi, K. Matsuda, *Nano Lett.* **2013**, *13*, 5944.
[32] M.-A. Stoeckel, M. Gobbi, T. Leydecker, Y.e Wang, M. Eredia, S. Bonacchi, R. Verucchi, M. Timpel, M. V. Nardi, E. Orgiu, P. Samorì, *ACS Nano* **2019**, *13*, 11613.
[33] K. Yokota, K. Takai, T. Enoki, *Nano Lett.* **2011**, *11*, 3669.
[34] S. Kobayashi, T. Nishikawa, T. Takenobu, S. Mori, T. Shimoda, T. Mitani, H. Shimotani, N. Yoshimoto, S. Ogawa, Y. Iwasa, *Nat. Mater.* **2004**, *3*, 317.
[35] S. Park, N. Mutz, T. Schultz, S. Blumenstengel, A. Han, A. Aljarb, L. J. Li, E. J. W. List-Kratochvil, P. Amsalem, N. Koch, *2D Materials* **2018**, *5*, 025003.
[36] A. Chaves, J. G. Azadani, H. Alsalman, D. R. da Costa, R. Frisenda, A. J. Chaves, S. H. Song, Y. D. Kim, D. He, J. Zhou, A. Castellanos-Gomez, F. M. Peeters, Z. Liu, C. L. Hinkle, S. H. Oh, P. D. Ye, S. J. Koester, Y. Lee, P. Avouris, X. Wang, T. Low, *npj 2D Mater. Appl.* **2020**, *4*, 28.
[37] D. Jena, A. Konar, *Phys. Rev. Lett.* **2007**, *98*, 136805.
[38] S. Grützmacher, M. Heyl, M. V. Nardi, N. Koch, E. J. W. List-Kratochvil, G. Ligorio, *Adv. Mater. Interfaces.* **2023**, *10*, 2300276.
[39] Y. Wang, M. Lieberman, *Langmuir* **2003**, *19*, 1159.
[40] H. Sugimuraa, K. Hayashia, N. Saitoa, N. Nakagirib, O. Takaia, *Appl. Surf. Sci.* **2002**, *188*, 403.
[41] S. R. Wasserman, G. M. Whitesides, I. M. Tidswell, B. M. Ocko, P- S. Pershan, J. D. Axe, *ACS* **1989**, *111*, 5853.
[42] O. M. Roscioni, L. Muccioli, A. Mityashin, J. Cornil, C. Zannoni, *J. Phys. Chem. C* **2016**, *120*, 14652.
[43] R. E. Geer, D. A. Stenger, M. S. Chen, J. M. Calvert, R. Shashidhar, *Langmuir* **1994**, *10*, 1171.
[44] J. Genzer, K. Efimenko, D. A. Fischer, *Langmuir* **2002**, *18*, 9307.
[45] Y. Gong, M. C. Wang, X. Zhang, H. W. Ng, B. D. Gates, *Langmuir* **2012**, *28*, 11790.
[46] M. F. Calhoun, J. Sanchez, D. Olaya, M. E. Gershenson, V. Podzorov, *Nat. Mater.* **2008**, *7*, 84.
[47] S. S. Israel, D. Rébiscoul, M. Odorico, V. Flaud, A. Ayral, *Langmuir* **2019**, *35*, 2792.
[48] M. Zhu, M. Z. Lerum, W. Chen, *Langmuir* **2012**, *28*, 416.
[49] Y. Wang, M. Lieberman, *ACS* **2003**, *19*, 1159.
[50] M. H. Park, Y. J. Jang, H. M. Sung-Suh, M. M. Sung, *Langmuir* **2004**, *20*, 2257.
[51] M.-H. Jung, H.-S. Choi, *Korean J. Chem. Eng.* **2010**, *26*, 1778.
[52] Y. Song, R. Premachandran Nair, M. Zou, Y. A. Wang, *Thin Solid Films* **2010**, *518*, 3801.
[53] D. Devaprakasam, S. Sampath, S. K. Biswas, *Langmuir* **2004**, *20*, 1329.
[54] D. J. Ellison, B. Lee, V. Podzorov, C. D. Frisbie, *Adv. Mater.* **2011**, *23*, 502.
[55] R. Bernasconi, A. Molazemhosseini, M. Cervati, S. Armini, L. Magagnin, *J. Electron. Mater.* **2016**, *45*, 5449.
[56] K. Hayash, N. Saito, H. Sugimura, O. Takai, N. Nakagiri, *Langmuir* **2002**, *18*, 7469.
[57] M. Heyl, D. Burmeister, T. Schultz, S. Pallasch, G. Ligorio, N. Koch, E. J. W. List-Kratochvil, *Physical Status Solidi (RRL)* **2020**, *14*, 2000408.
[58] M. Heyl, E. J. W. List-Kratochvil, *Appl. Phys. A* **2022**, *129*, https://doi.org/10.1007/s00339-022-06297-z.
[59] S. Najmaei, X. Zou, D. Er, J. Li, Z. Jin, W. Gao, Q.i Zhang, S. Park, L. Ge, S. Lei, J. Kono, V. B. Shenoy, B. I. Yakobson, A. George, P. M. Ajayan, J. Lou, *Nano Lett.* **2014**, *14*, 1354.
[60] D.-H. Lien, S. Z. Uddin, M. Yeh, M. Amani, H. Kim, J. W. Ager, E. Yablonovitch, A. Javey, *Science* **2019**, *364*, 468.
[61] D. Vaquero, V. Clerico, J. Salvador-Sanchez, A. Martin-Ramos, E. Diaz, F. Dominguez-Adame, Y. M. Meziiani, E. Diez, J. Quereda, *Commun. Phys.* **2020**, *3*, 3.
[62] H. Shi, R. Yan, S. Bertolazzi, J. Brivio, B. Gao, A. Kis, D. Jena, H. G. Xing, L. Huang, *ACS Nano* **2013**, *7*, 1072.
[63] M. Heyl, S. Grützmacher, S. Rühl, G. Ligorio, N. Koch, E. J. W. List-Kratochvil, *Adv. Mater. Interfaces.* **2022**, *9*, 2200362.
[64] A. Gurarslan, Y. Yu, L. Su, Y. Yu, F. Suarez, S. Yao, Y. Zhu, M. Ozturk, Y. Zhang, L. Cao, *ACS Nano* **2014**, *8*, 11522.
[65] M. J. Frisch, G. W. Trucks, H. B. Schlegel, G. E. Scuseria, M. A. Robb, J. R. Cheeseman, G. Scalmani, V. Barone, G. A. Petersson, H. Nakatsuji, X. Li, M. Caricato, A. Marenich, J. Bloino, B. G. Janesko, R. Gomperts, B. Mennucci, H. P. Hratchian, J. V. Ortiz, A. F. Izmaylov, J. L. Sonnenberg, D. Williams-Young, F. Ding, F. Lipparini, F. Egidi, J. Goings, B. Peng, A. Petrone, T. Henderson, D. Ranasinghe, et al., *Gaussian 09 v. C.01*, Gaussian, Inc, Wallingford CT, **2016**.